

Preparation and characterisation of iron substituted $Mn_{1.7}Cu_{1.3-x}Fe_xO_4$ spinel oxides ($x = 0, 0.1, 0.3, 0.5$)

Justyna Ignaczak^{1*}, Yevgeniy Naumovich², Karolina Górnicka³, Jan Jamroz⁴, Wojciech Wróbel⁴, Jakub Karczewski³, Ming Chen⁵, Piotr Jasiński¹, Sebastian Molin¹

¹ Faculty of Electronics, Telecommunications and Informatics, Gdańsk University of Technology,
ul. G. Narutowicza 11/12, 80-233 Gdańsk, Poland

² Department of High Temperature Electrochemical Processes, Institute of Power Engineering,
ul. Augustówka 36, 02-981 Warsaw, Poland

³ Faculty of Applied Physics and Mathematics, Gdańsk University of Technology,
ul. G. Narutowicza 11/12, 80-233 Gdańsk, Poland

⁴ Faculty of Physics, Warsaw University of Technology, ul. Koszykowa 75, 00-662 Warsaw, Poland

⁵ Department of Energy Conversion and Storage, Technical University of Denmark, Fysikvej, 2800 Kgs.
Lyngby, Denmark

*corresponding author: justyna.ignaczak@pg.edu.pl

Abstract

Spinel oxides with the general formula $Mn_{1.7}Cu_{1.3-x}Fe_xO_4$ ($x = 0, 0.1, 0.3, 0.5$) were prepared and evaluated in this work for their properties at high temperatures. The effect of partially substituting Cu by Fe has not been studied so far for this group of materials and is thus evaluated in this work.

$Mn_{1.7}Cu_{1.3-x}Fe_xO_4$ powders were synthesised by a soft chemistry process and studied in terms of crystallographic phase analysis, electrical conductivity, thermal expansion, and sinterability behaviour. The results show that the Fe content has a significant influence on the phase composition and the resulting properties. Characterisation of the dilatometry and conductivity coupled with XRD phase analysis across a wide temperature range allowed the relations between the materials properties and compositions to be observed. The results indicate that $Mn_{1.7}Cu_{0.8}Fe_{0.5}O_4$ is a promising material for use as a protective coating for interconnects in intermediate temperature Solid Oxide Fuel Cells.

29 Introduction

30 Spinel oxides form a remarkable group of ceramic materials with a wide range of potential applications
31 [1]. The general formula of a “regular” spinel is AB_2O_4 with either a cubic or tetragonal structure, where
32 A is a divalent cation, and B is a trivalent cation, which occupy tetrahedral and octahedral sites,
33 respectively. The spinel mineral is $MgAl_2O_4$, which has a regular structure. A spinel can also adopt an
34 “inverse” structure, where half of the trivalent B cations occupy the tetrahedral sites, and the divalent
35 A cations and the remaining half of the B cations occupy the octahedral sites. Due to these broad
36 possibilities, many different spinel materials can be synthesised. Indeed, spinels have found wide use
37 in Li-ion batteries as electrodes [2], supercapacitor electrodes [3], thermal barrier coating material [4],
38 as well as in other devices [5–7]. Depending on the chemical composition as well as on the preparation
39 method/thermal history, spinels can be characterised by a broad range of electrical transport
40 properties. It was reported that the electronic conductivity of a spinel occurs mainly by electron
41 hopping between octahedral sites [8,9], and the cation arrangement can depend on the thermal
42 history of the sample.

43 Manganese-copper-based spinels are interesting materials that have been studied for range of
44 important applications [10–13]. The abundance and low toxicity of Mn and Cu makes the material of
45 interest, especially as a possible replacement of Mn-Co-based spinels, where the mining issues and
46 toxicity of cobalt are problematic. Mn-Cu spinels are already recognised as a potential catalyst for the
47 steam reforming of methanol [14], as a ceramic film for spectrally selective solar-derived
48 applications [15], and also as a protective coating on the interconnects in solid oxide fuel cells [16].

49 The phase diagram of Mn-Cu-O shows that a pure spinel phase forms only in a relatively narrow
50 compositional and temperature window [17,18]. For this reason, most studied compositions have
51 focused on Mn_2CuO_4 or a slightly modified $Mn_{1.7}Cu_{1.3}O_4$ [19–21]. A increased Cu content shifts the
52 compositions towards a mixture of spinel and CuO, whereas a decreased Cu content, towards a mixture
53 of manganese oxide and spinel.

54 Petric and Ling investigated the electrical conductivity of $Mn_{1.7}Cu_{1.3}O_4$, which achieved a very high value
55 of 225 S/cm at 750 °C [22]. This is much higher than the electrical conductivity reported for the widely
56 used $MnCo_2O_4$ spinel ($\sim 60 \text{ S cm}^{-1}$ at 800 °C). Since this work, interest in Mn-Cu spinels has increased.
57 They have been tested as a protective coating for steel interconnects, and as a contacting mesh
58 element in high temperature fuel cells [23–26].

59 Partial substitution of one of the cations is a well-known way to improve the properties of spinel-based
60 ceramics. This approach has been extensively used to tailor the properties of $MnCo_2O_4$ spinels. Partial

61 substitution of Co by either Fe or Cu has been reported to influence the electrical conductivity and
62 thermal expansion [27–29]. Talic et al. showed that the addition of iron ($\text{MnCo}_{1.5}\text{Fe}_{0.5}\text{O}_4$) decreased the
63 electrical conductivity and the thermal expansion coefficient, whereas the addition of Cu
64 ($\text{MnCo}_{1.5}\text{Cu}_{0.5}\text{O}_4$) resulted in higher electrical conductivity and a higher thermal expansion
65 coefficient [30]. Other studies considered the effect of the addition of Fe/Cu on high temperature
66 corrosion and chromium evaporation of steel interconnects [31–34].

67 The effects of elemental substitutions in Mn-Cu-based spinels have been studied to a much lesser
68 extent. Bhandage et al. have studied a $\text{Cu}_x\text{Cd}_{1-x}\text{Mn}_2\text{O}_4$ system [11]. For $x = 1$, pure cubic phase spinel
69 was obtained, whereas for a composition with $x < 0.5$, a tetragonal phase was found. The same author
70 also studied the $\text{Ni}_x\text{Cu}_{1-x}\text{Mn}_2\text{O}_4$ system [12]. Ni substitution in the Mn-Cu spinel was considered as a
71 protective coating and for its effect on high-temperature corrosion protection by Joshi and Petric [35].
72 Ni stabilised the cubic spinel phase and resulted in a small decrease of electrical conductivity.

73 A number of synthesis methods have been used for the preparation of different spinel powders,
74 including modified sol-gel [36,37], EDTA gel [38], the glycine nitrate process [39], spray pyrolysis
75 [28,30], co-precipitation [40], and solid state [41,42]. Among the reported methods, the sol-gel-derived
76 routes seem to offer the advantage of cation mixing at the atomic level leading to high homogeneity
77 and formation of small particle sizes [43].

78 In the present investigation, the $\text{Mn}_{1.7}\text{Cu}_{1.3}\text{O}_4$ spinel was used as the starting material, and its
79 derivatives with partial substitution of Cu by Fe were studied. The influence of iron substitution on its
80 properties, related to SOFC interconnect protection, namely sintering behaviour, crystal structure, and
81 electrical conductivity was evaluated.

82

83 **2. Experimental**

84 **2.1. Powder preparation**

85 Spinel powders with the general formula $\text{Mn}_{1.7}\text{Cu}_{1.3-x}\text{Fe}_x\text{O}_4$, where $x=0, 0.1, 0.3, \text{ and } 0.5$, were
86 synthesised by a modified Pechini method [44]. Throughout the paper, the powders and sample
87 compositions are abbreviated according to Table 1. The starting substrates used in the syntheses were
88 hydrated nitrate salts of metals: manganese (II) nitrate ($\text{Mn}(\text{NO}_3)_2 \cdot 4\text{H}_2\text{O}$, Sigma Aldrich, $\geq 97\%$), copper
89 (II) nitrate ($\text{Cu}(\text{NO}_3)_2 \cdot \text{H}_2\text{O}$, Sigma Aldrich, 99.999%), and iron (III) nitrate ($\text{Fe}(\text{NO}_3)_3 \cdot 9\text{H}_2\text{O}$, Sigma Aldrich,
90 99.999%). Water solutions of dissolved nitrates with known concentrations (pre-standardised
91 thermogravimetrically) were mixed together in the proper molar ratio corresponding to the intended

92 nominal composition of the spinel powders. The water solutions containing all of the desired cations
93 were heated under constant stirring to 80 °C (controlled using an insertion probe) on a magnetic
94 stirring hot plate. Citric acid (C₆H₈O₇, Sigma Aldrich, 99%), and EDTA ([CH₂N(CH₂CO₂H)₂]₂, Sigma Aldrich,
95 99%) were added to the solution under stirring as chelating agents in the molar ratio 2:1:1-TMI (total
96 molar ions). To control the pH at the desired level of 8, diluted ammonia (25% aqueous solution) was
97 added dropwise. To start the transesterification process, ethylene glycol (C₂H₆O₂, Sigma Aldrich, 98%)
98 was added under continuous stirring, in the amount to obtain a ratio of 1 mol of polyalcohol to 1 mol
99 of metal cations. The liquid precursor was then held at 80 °C until a dense gel-like structure was
100 obtained. It was further dried at 130 °C for 4 h. The resulting material was placed in a muffle furnace
101 and heated to 400 °C for 2 h. The obtained powder was ground in an agate mortar and further calcined
102 at 900 °C for 2 h. In the end, the powders were again ground in the agate mortar and used for further
103 studies.

104

105 **2.2. Pellet preparation**

106 Ceramic pellets were prepared from the synthesised powders by uniaxial pressing in a hydraulic press
107 (Carver, USA). The powders were compacted using 54 MPa pressure. The obtained disk-shaped green
108 bodies had a diameter of ~16 mm and a thickness of 1.5–2 mm. The pressed pellets were sintered at
109 three different temperatures: 900 °C, 1000 °C, and 1100 °C in air. Heating and cooling rates of
110 3.6 °C min⁻¹ were used with a dwell time of 2 h. The dimensions of the sintered pellets were measured
111 (using a Mitutoyo micro-caliper) to calculate the linear shrinkage. The porosity of the sintered pellets
112 was determined from analyses of SEM images of polished cross-sections. For each sample, ten images
113 were taken at the same magnification, and these images were analysed using the ImageJ software [44].

114

115 **2.3. Materials characterisation**

116 The x-ray diffraction (XRD) technique was used to determine the phase composition and the crystal
117 structure of the fabricated powders. The measurements of the synthesised powders were conducted
118 at room temperature using a Bruker D2 Phaser 2nd generation diffractometer with CuK α radiation
119 ($\lambda = 1.5404 \text{ \AA}$) and XE-T detectors. Data were collected from $2\theta = 10^\circ$ to 90° with a step size of 0.01°
120 and accounting time of 0.2 sec for each step. The results were processed by means of LeBail refinement
121 using the Bruker Topas software.

122 High temperature X-ray powder diffraction data were collected on a Philips X'Pert Pro diffractometer,
123 fitted with an X'Celerator detector, using Ni filtered Cu-K α radiation ($I_1 = 1.54056 \text{ \AA}$ and $I_2 = 1.54439 \text{ \AA}$).
124 Elevated temperature measurements were performed using an Anton-Paar HTK 1200 high

125 temperature camera. Data were collected in flat plate θ/θ geometry on a Pt-coated sample holder.
126 Calibration was carried out with an external LaB_6 standard. Diffraction patterns were acquired at room
127 temperature and at 50 °C intervals from 50 °C to 850 °C in air. Data at room temperature and at 850 °C
128 were collected over the range 5–105° 2θ , in steps of 0.033°, with an effective scan time of 120 s per
129 step. Shorter scans were performed for intermediate temperatures with an effective scan time of 40 s
130 per step.

131 Thermogravimetric analysis (TGA) of the studied oxides was performed using a Netzsch TG 209 F3
132 Tarsus thermobalance. The measurements were carried out both in air and argon atmospheres. The
133 mass change was observed up to 900 °C with a heating and cooling rate of 3 °C min^{-1} .

134 Dilatometric studies of the sintering and thermal expansion were carried out using a Netzsch DIL402
135 dilatometer. Measurements were performed in a synthetic air atmosphere with a heating rate of 5 °C
136 min^{-1} , with a 15 minutes isothermal step at 1100 °C and a cooling rate of 3 °C min^{-1} .

137 The phase diagram of Cu-O₂ was calculated using the FACTSAGE software and databases [45].

138 Scanning electron microscopy (SEM) investigation of the powders and pellet cross sections were
139 carried out on a Phenom XL (Thermo Fisher Scientific) desktop SEM equipped with an integrated
140 energy dispersive X-ray (EDX) microanalyser. For preparation of the pellet cross sections, samples were
141 mounted in epoxy (EpoFix, Struers) and then polished on a semi-automatic Struers Tergamin-20
142 machine down to a 1 μm finish.

143 The electrical conductivity of the pellets was estimated by employing the van der Pauw method [46].
144 The samples were heated to 900 °C and measured down to 200 °C with decrements of 50 °C in air. The
145 activation energy, E_a , was calculated using the formula, derived from the Arrhenius equation:

146
$$\ln\sigma T = \frac{-E_a}{k} \times \frac{1}{T} + \ln\sigma_0, \quad (\text{Eq.1})$$

147 where σ — electrical conductivity, T — temperature, σ_0 — pre-exponential factor, E_a — activation
148 energy, and k — Boltzmann's constant.

149 Electrical conductivity data were corrected for sample porosity with using the Brueggemann
150 asymmetric model, according to the following formula [47]:

151
$$\sigma = \sigma_m \cdot \frac{1}{(1-p)^{\frac{3}{2}}}$$

152 Where σ is the corrected conductivity, σ_m is the measurement conductivity and p is sample porosity.

153

154

155

156 3. Results and discussion

157 3.1. Chemical, microstructural and sintering characterisation of the powders

158 Chemical and morphological analysis of the powders

159 After the milling process, the powders were characterised for their elemental compositions,
 160 morphologies, and phase structures. EDX analyses were performed on the powders to determine the
 161 atomic compositions of the calcined powders. The results of the analyses are presented in Table 1
 162 (with the accuracy of EDX method +/- 1%). The calculated Mn/(Mn+Fe) and Fe/(Fe+Cu) cation ratios
 163 correspond well to the expected stoichiometries.

164

165 **Table 1.** Chemical composition of powders determined by means of EDX and sample's names used in
 166 this paper.

Desired composition	Sample name	Metal ratio			Mn / Cu+Fe	Fe / Fe+Cu	Corresponding spinel composition
		Mn	Cu	Fe			
$Mn_{1.7}Cu_{1.3}O_4$	0Fe	0.56	0.44	-	1.27	-	$Mn_{1.68}Cu_{1.32}O_4$
$Mn_{1.7}Cu_{1.2}Fe_{0.1}O_4$	01Fe	0.59	0.38	0.03	1.43	0.07	$Mn_{1.73}Cu_{1.15}Fe_{0.12}O_4$
$Mn_{1.7}Cu_{1}Fe_{0.3}O_4$	03Fe	0.56	0.34	0.10	1.27	0.23	$Mn_{1.69}Cu_{0.99}Fe_{0.32}O_4$
$Mn_{1.7}Cu_{0.8}Fe_{0.5}O_4$	05Fe	0.57	0.25	0.18	1.32	0.42	$Mn_{1.69}Cu_{0.76}Fe_{0.54}O_4$

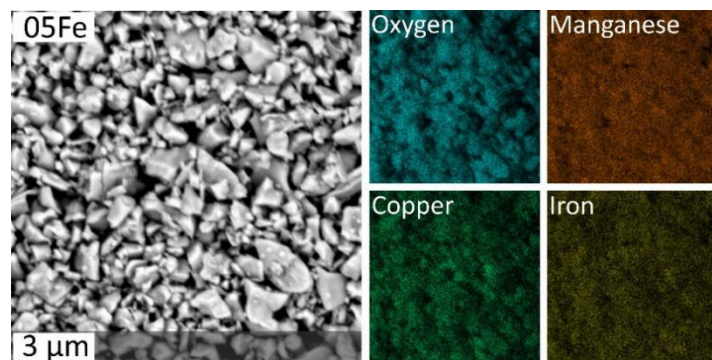
167

168 Figure 1 presents a representative SEM micrograph of the 05Fe powder after calcination at 900 °C and
 169 after milling in an agate mortar. All of the powders were composed of micron-sized particles (~1–3 μm)
 170 without the presence of larger agglomerates. No influence of iron substitution on the particle size
 171 could be observed.

172

173





174

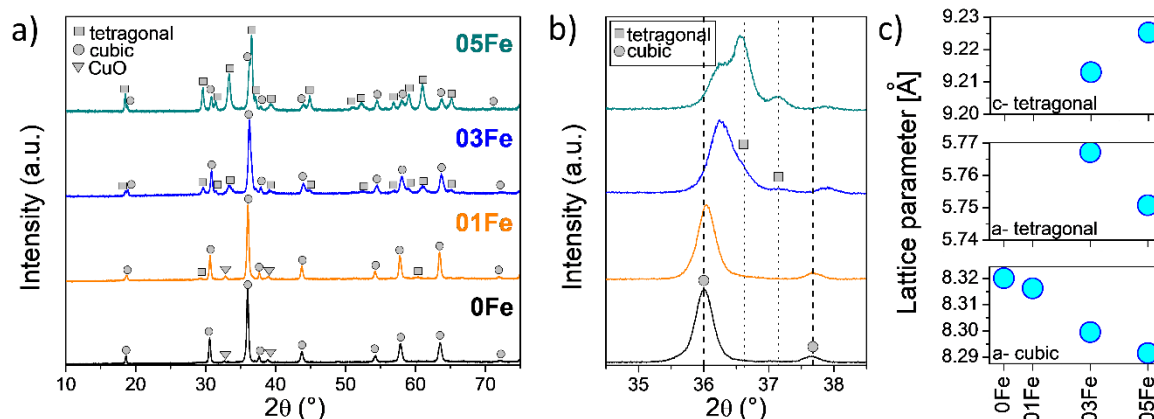
175 **Figure 1.** Scanning electron microscopy image and energy dispersive elemental analysis of the 05Fe
 176 $(\text{Mn}_{1.7}\text{Cu}_{0.8}\text{Fe}_{0.5}\text{O}_4)$ powder.

177 **Room-temperature XRD analysis of the powders**

178 The room temperature XRD patterns of the calcined powders are shown in Figure 2a (full measured
 179 range) and 2b (enlargement of the main peak region). The non-substituted 0Fe powder revealed the
 180 existence of a cubic spinel phase (space group $Fd\text{-}3m$, ICDD card #35-1030) with a possible very small
 181 addition of CuO (estimated to <3 vol.%, monoclinic structure, space group $c2/c$, #45-937). The
 182 observation of these two phases is in agreement with the Cu-Mn-O phase diagram, where single-phase
 183 cubic might decompose at low temperatures to spinel + MnO_2 , or to $\text{MnO}_2 + \text{CuO}$ [17,18,20]. A quite
 184 similar structure was observed for the 01Fe powder. Only the cubic spinel and a small amount of
 185 another phase could be seen. It must be noted that the peaks ascribed to CuO might also have been
 186 caused by the cubic (#35-1030) or tetragonal (CuMn_2O_4 , #71-1141) spinel phase. Due to overlapping
 187 peaks and small relative intensity, the exact determination of the minority phase is not possible. The
 188 presence of minor phase impurities in $\text{Cu}_{1.3}\text{Mn}_{1.7}\text{O}_4$ is known in the literature, for example, Bobruk
 189 et al. observed the same level of CuO-attributed peaks in this material, synthesised by EDTA-gel
 190 processes and calcined at 700 °C [38]. The introduction of iron shifted the $\sim 36^\circ$ peak position towards
 191 the higher 2θ angle, evidencing contraction of the unit cell, compliant with a smaller size of the Fe
 192 cations than Cu cations.

193 The increase in Fe-content resulted in the formation of a new phase, which can be attributed to a
 194 tetragonal spinel structure (space group: $I41/amd:2$) [48]. No indications of iron oxides could be found
 195 in the spectra either. For the 03Fe powder, the cubic spinel peak had the highest intensity, whereas
 196 for the 05Fe powder, the tetragonal phase dominated.





197

198 **Figure 2.** X-ray diffraction patterns of powders synthesised via the EDTA-CA gel process after
 199 calcination at 900 °C (a, b). Lattice parameters (at room temperature), determined by structure
 200 fitting of XRD patterns for spinel powders calcined at 900 °C (c).

201

202 The lattice parameters determined by structure fitting of the cubic Fd-3m space group and tetragonal
 203 I41/amd:2 are plotted in Figure 2c and summarised in Table 2. The cubic spinel phase changed the unit
 204 cell size (“a” parameter) linearly with the substitution of copper with iron. For the tetragonal phase,
 205 the unit cell size showed a more complex behaviour. The “a” parameter decreased its value, whereas
 206 the “c” parameter increased.

207 The formation of the tetragonal phase in the Mn-Cu spinel can be explained by the Jahn-Teller effect,
 208 i.e. the elongation of the octahedral in the “c” direction [49]. This was caused by the presence of
 209 octahedrally coordinated Mn³⁺ cations (or possibly also Cu²⁺) [49,50]. Mn-Cu spinels are interesting as
 210 materials which contain two Jahn-Teller ions: Mn³⁺ and Cu²⁺[18]. Baffier and Huber argued that for the
 211 formation of a tetragonal structure, the relative concentration of Mn³⁺ ions needs to be high, i.e. >50%
 212 of the sites [10,51]. The addition of iron thus resulted in the formation of Mn³⁺ in octahedral positions
 213 (or Cu²⁺), which allowed for the incorporation of the copper cations into the spinel structure. The
 214 elongation of the unit cell in one direction (“c”) was followed by contraction of the unit cell in the “a”
 215 direction.

216 The effect of cation substitution in the spinel structure cannot be resolved simply due to the complexity
 217 of the structure, i.e. the presence of tetrahedral and octahedral positions and multiple possible valence
 218 states of the cations. Due to the multitude of the possible arrangements and cation sizes, it is hard to
 219 determine where the newly introduced cations are situated. As evidenced by XRD, partial substitution
 220 of Cu by Fe led to the decrease of the lattice parameter “a”, as shown in Table 2. In general, iron cations

221 are smaller than copper cations, so a decrease of the cell-size parameter can be expected. Manganese
 222 has a strong tendency to occupy the octahedral position. Due to the high Cu content in the $Mn_{1.7}Cu_{1.3}O_4$
 223 spinel, some Cu should also occupy the octahedral position, with the remaining Cu in the tetrahedral
 224 position. The situation is also complicated by the fact that, at room temperature, the compositions rich
 225 in iron (03Fe and 05Fe) are not single phase — they form a mixed cubic-tetragonal oxide, where the
 226 cations' distributions will be further confounded. Therefore, in this paper, we do not propose any
 227 specific cationic distribution, as it is far too complex and uncertain in our view. A summary of the
 228 reported possible cation distributions in the Mn-Cu spinels can be found in [18].

229

230 **Table 2.** Lattice parameters for cubic and tetragonal phases determined by Le Bail refinement (at
 231 room temperature).

Powder	Phase:	Cubic	Tetragonal			
		a_c [Å]	a_T [Å]	a_T' [Å]	c_T [Å]	c_T / a_T'
0Fe	C	8.3201(5)				
01Fe	C	8.3162(1)				
03Fe	C+T	8.2995(4)	5.7672(2)	8.13175	9.2133(2)	1.13
05Fe	C+T	8.2915(6)	5.7508(3)	8.1086	9.2253(4)	1.14

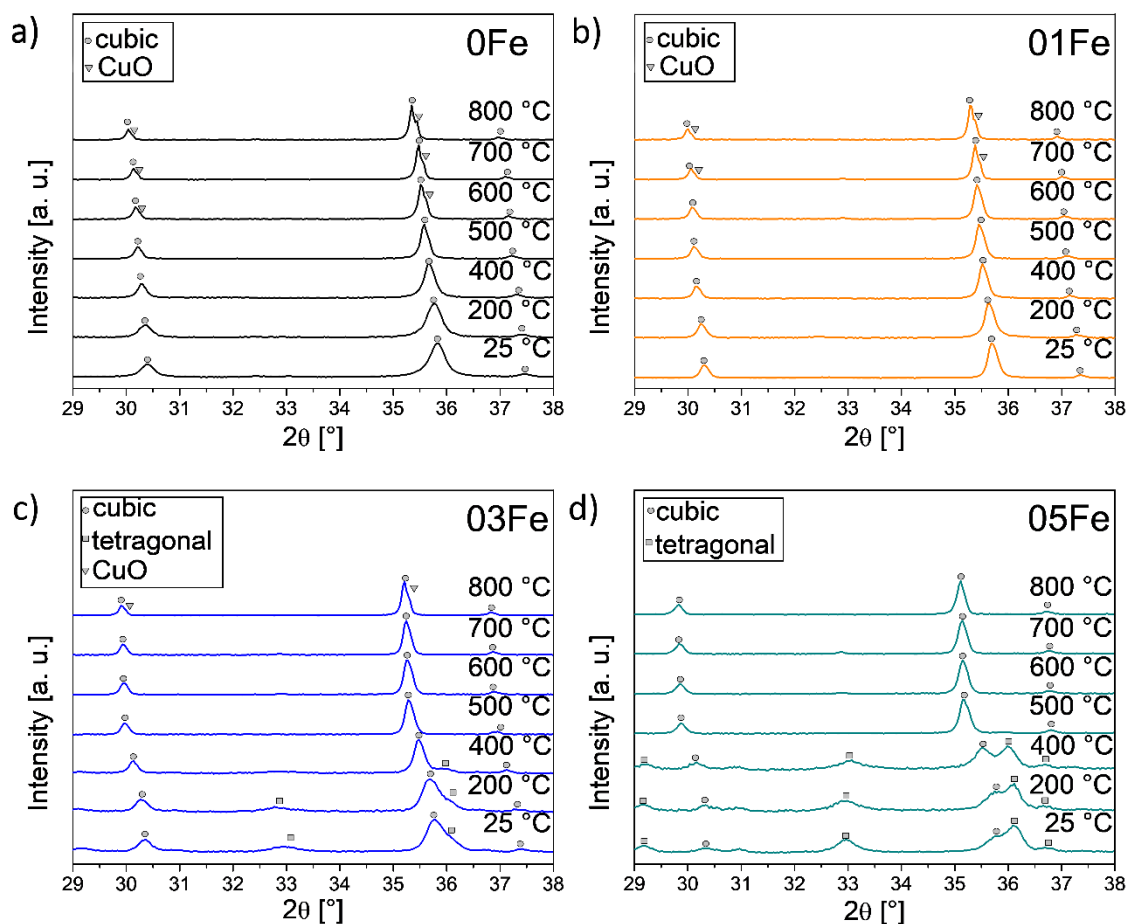
232

233 High-temperature XRD analysis of the powders

234 In order to follow the development of the phase-composition of the materials vs. temperature, in-situ
 235 high-temperature XRD analyses were performed. The results are presented in Figure 3a–d.

236 For the 0Fe and 01Fe, the cubic phase did not change upon heating. Above 500 °C, the occurrence of
 237 a new phase could be noticed for both powders. It is ascribed to CuO, which is in line with the phase
 238 diagram [17] and discussion by Martin and Petric [20]. According to the phase diagram, the pure spinel
 239 phase was stable in only a quite narrow temperature window (roughly between 500 °C and 600 °C).
 240 For the 03Fe and 05Fe powders, where the cubic and tetragonal phases co-existed at room
 241 temperature, transformation into a single cubic phase was observed at >400 °C. In the case of the 05Fe
 242 powder, the tetragonal phase remained stable at 400 °C, whereas for the 03Fe powder, it seemed to
 243 disappear at 400 °C. CuO also seemed to form in the 03Fe powder, whereas it was not detected in the
 244 05Fe powder. The addition of Fe stabilised the spinel phase, which was a mixture of tetragonal-cubic
 245 below 500 °C and transformed into a fully cubic spinel at >500 °C.



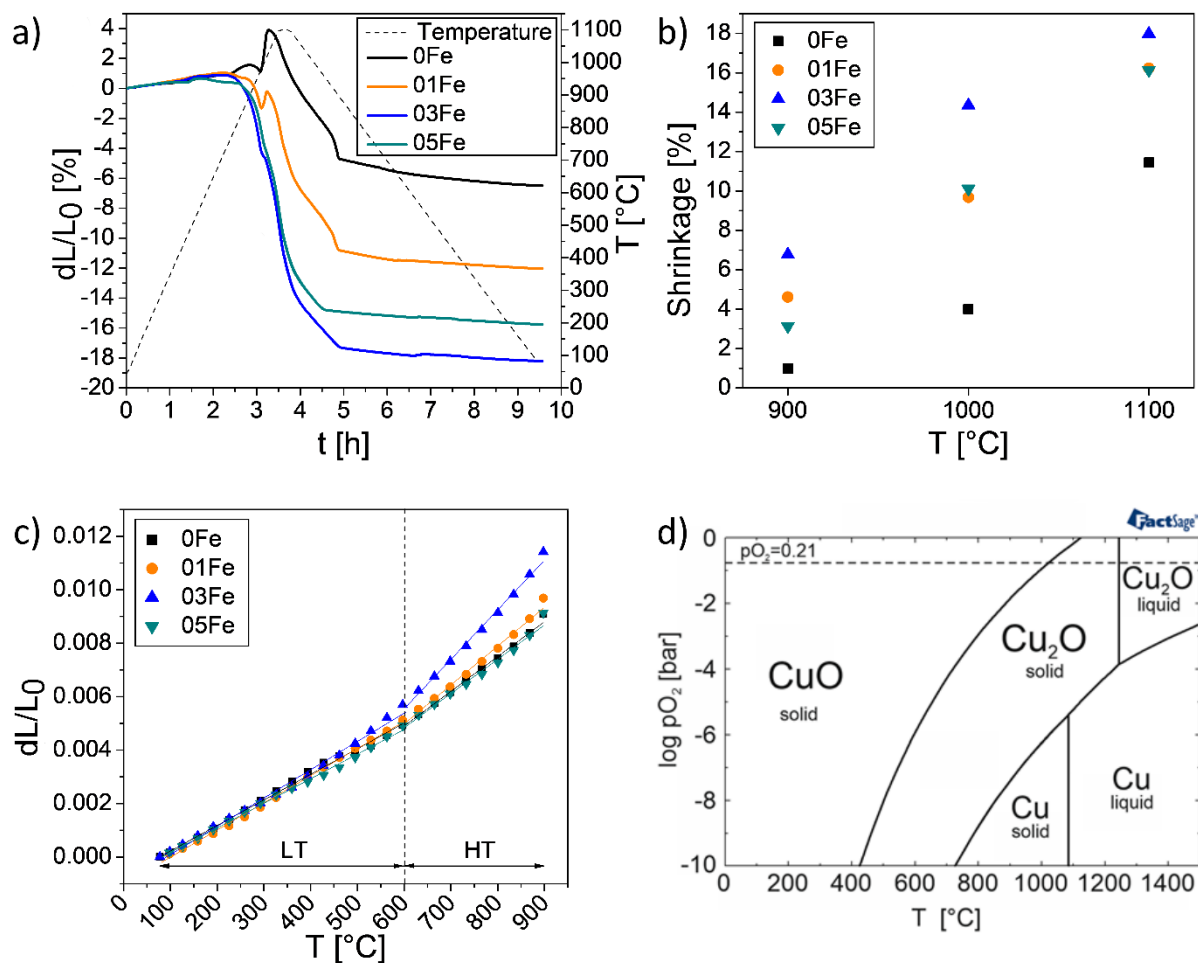


246

247 **Figure 3.** High-temperature XRD (25–800 °C in air) patterns for the powders: 0Fe(a), 01Fe (b), 03Fe
 248 (c), and 05Fe (d).

249 **Dilatometry study**

250 Following the phase characterisation was the determination of the sintering properties of the prepared
 251 compounds. A dilatometry study was performed in order to determine the shrinkage profiles of the
 252 compacted powders (up to 1100 °C) and thermal expansion coefficient (TEC) values. In addition to the
 253 measurements performed in the dilatometer, the diameters of the pellets were analysed before and
 254 after ex-situ sintering in a furnace at different temperatures (900 °C, 1000 °C, and 1100 °C). The
 255 dilatometry curves and values of relative shrinkage for the pellets are presented in Figure 4a–c.



256

257 **Figure 4.** Dilatometry results (in air) for sintering of the powders (a), relative shrinkage of the pellets
 258 measured after sintering the green bodies at 900 °C, 1000 °C, 1100 °C (b), thermal expansion of the
 259 spinel pellets, pre-sintered at 1100°C (cooling cycle from 900 °C in air) (c), and phase diagram of Cu-
 260 O₂ showing the phase change of CuO to Cu₂O (d).

261

262 The sintering behaviour of the materials differed considerably (Figure 4a). Intense expansion was
 263 visible, especially for the non-iron-doped spinel, upon heating at ~1000 °C. The sample expanded by
 264 ~4% within a few minutes, and then the sintering began. Quite similar behaviour was visible for the
 265 01Fe powder, but to a smaller extent, potentially due to the earlier onset of sintering, as the sample
 266 started to sinter at ~850–900 °C. The observed behaviour can be attributed to reduction of the CuO
 267 phase, which formed upon heating of the spinel, as described in the HT-XRD discussion (see Figure 3).
 268 CuO phase reduced into the Cu₂O phase in this temperature range (~1000 °C), well in line with the Cu-
 269 O-temp phase diagram presented in Figure 4d and the literature [52,53]. For the 03Fe and 05Fe
 270 materials, where less or no CuO was detected in the XRD spectra, no such peaks in the dilatometry

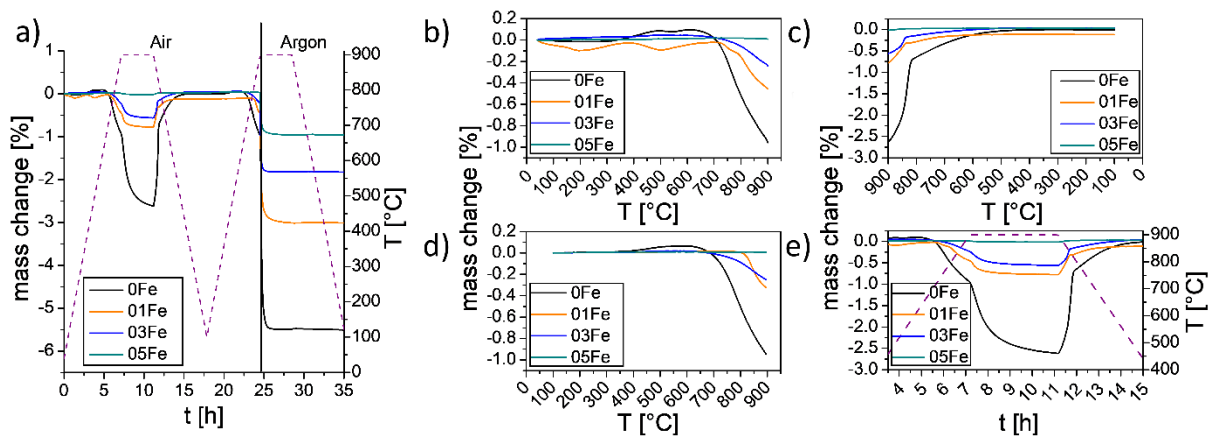
271 curves were visible. These powders started to sinter at ~ 800 °C and followed a regular sintering
272 pattern. The largest shrinkage was observed for the 03Fe sample ($\sim 18\%$), followed by the 05Fe sample
273 ($\sim 16\%$). The continuous dilatometry results were confirmed by the ex-situ pellet diameter
274 measurements: the smallest shrinkage was obtained for the 0Fe samples, followed by 01Fe and 05Fe,
275 while the largest shrinkage was obtained for the 03Fe sample. The shrinkage values (Figure 4 b)
276 demonstrate that iron doping sufficiently enhanced the sinterability of the studied materials, however
277 fabrication of the ceramics with low porosity in air required temperatures above 1000 °C.

278 Thermal expansion coefficients were determined using data collected during cooling of the samples
279 from 900 °C (samples were sintered in air at 1100 °C). As the curves were not linear in the 50–900 °C
280 temperature range, the analysis region was divided into high temperature (600–900 °C) and low
281 temperature (50–600 °C) intervals. The calculated TEC values are presented in Table 5. For the high
282 temperature domain, thermal expansion demonstrated a complex effect of the iron doping, with an
283 apparent maxima for the 03Fe ceramic. In the low temperature region, all of the sintered samples had
284 a TEC of $9.2\text{--}10.6 \times 10^{-6} \text{ K}^{-1}$. In general, iron substitution did not have a strong influence on the thermal
285 expansion.

286 **Thermogravimetric analysis**

287 In addition to dilatometry, thermogravimetric analyses were performed. TGA revealed that $\text{Mn}_{1.7}\text{Cu}_{1.3-}$
288 xFe_xO_4 complex oxides demonstrated sufficient activity in oxygen exchange with the environment
289 (Figure 5a–e). For the 0Fe, upon heating from room temperature to 900 °C, the sample initially gained
290 weight ($\sim 0.05\%$), which started at ~ 400 °C, then at around 700 °C it started losing weight (Figure 5b
291 first cycle of heating, and Figure 5d second cycle of heating). The sample with no iron was the only one
292 to show no notable weight increase upon heating. The addition of iron suppressed the weight loss
293 effect. For the 01Fe and 03Fe, the weight loss started at ~ 700 °C and had a much smaller extent than
294 the weight loss of the 0Fe. For the 0Fe powder, at isothermal hold at 900 °C, the weight change had
295 not stabilised after 2 hours, which indicates relatively slow equilibration. The 01Fe and 03Fe powders
296 seemed to stabilise their weight change faster (Figure 5e). For the 05Fe sample, neither weight gain
297 nor weight loss was found. The 05Fe powder was practically inert in air, which supports the expectation
298 of good stability in oxidising atmospheres at high temperatures. When cooling (Figure 5d), the mass
299 change process was reversible, which confirms that this phenomenon is related to the stability of the
300 tested materials and the oxidising atmosphere. The weight loss can be explained as a result of the
301 formation of a CuO phase: the O/Cu ratio was lower in the CuO than in the spinel, therefore
302 segregation of the CuO resulted in net loss of weight. At high temperature (~ 900 °C) the reduction of
303 CuO to Cu_2O is also possible, visible in Figures 5c and 5e, in-line with the phase diagram presented in

304 Figure 4d. The weight loss trend corresponds well with the amount of possible CuO formation: for the
 305 05Fe, where no CuO was detected upon heating, there was no weight loss, and the sample was stable
 306 upon heating, while for the 0Fe, it was very prominent. One can note that the behaviour of the 03Fe
 307 demands presence of traces of CuO, confirming the XRD observation. This might explain the behaviour
 308 of the dilatometric curve for this material as well as its electric conductivity: the amount of iron in the
 309 03Fe was not sufficient to keep the Cu in the cubic phase, so CuO particles grew during heating, which
 310 led to the rise of the TEC and changes in electrical conductivity.



311
 312
 313 **Figure 5.** Mass change of the Mn_{1.7}Cu_{1.3-x}Fe_xO₄ powders in air as a function of time (a), first heating
 314 ramp (b), first cooling ramp (c), second heating ramp (d), and isothermal hold after first heating ramp
 315 (e).

316 3.2. Electrical conductivity characterisation of the spinels

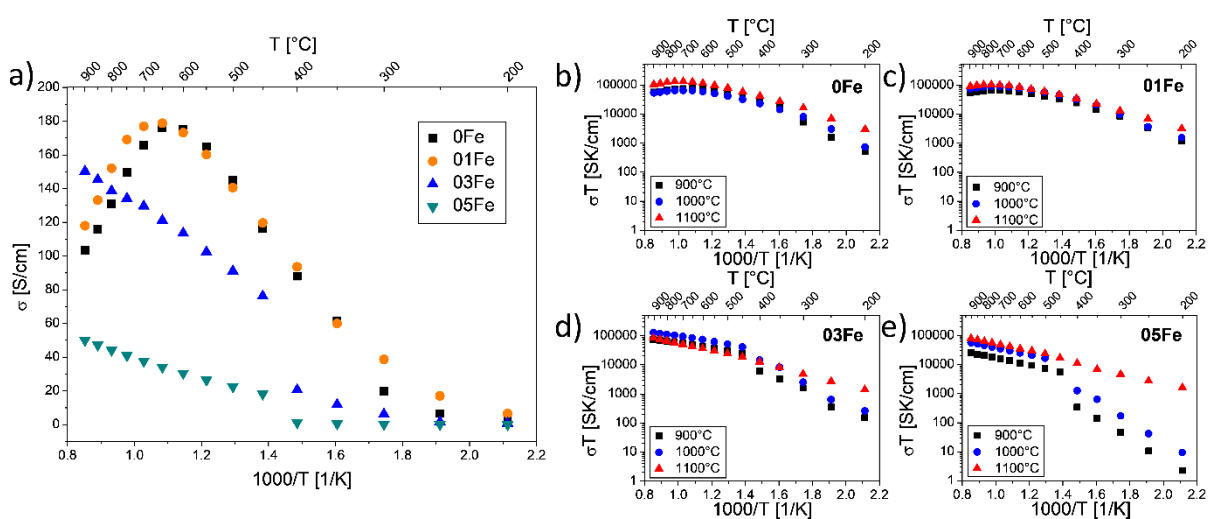
317 The electrical properties of the materials were analysed by studying the DC electrical transport
 318 properties of the sintered pellets in air in the temperature range 900–200 °C. To evaluate the effects
 319 of porosity and thermal treatment in general, pellets prepared from the 0Fe, 01Fe, 03Fe and 05Fe
 320 powders were sintered at either 900 °C, 1000 °C, or 1100 °C in air. The results of the measurements
 321 are presented in Figure 6a–e.

322 The behaviour of the samples depended on the iron substitution level, as summarised in Figure
 323 6a. For the sample without iron (0Fe, Figure 6b) and with low iron content (01Fe, Figure 6c), the
 324 electrical behaviour was notably different than for the samples with higher iron content (03Fe and
 325 05Fe, Figures 6d and 6e, respectively). For the 0Fe and 01Fe, the maximum electrical conductivity was
 326 reached at ~650 °C. The maximum conductivity value was quite similar, reaching ~180 S cm⁻¹, which
 327 can be considered very high (the small difference between the samples is within the experimental
 328 error margin of ±5%). Below the maximum, the conductivity was thermally activated, whereas above
 329 the maximum, the conductivity decreased with temperature increase. The point (temperature) of

330 conductivity maximum coincided with the point where the spinels started losing weight. This was thus
 331 also connected to the formation of the CuO phase. Similar effects have been described by Martin and
 332 Petric [20]. They also measured thermopower and determined that the majority of carriers are
 333 electron holes (p-type conductivity).

334 For the samples with higher iron content, i.e. the 03Fe and 05Fe, the conductivity exhibited a clear
 335 transition point, where the levels of electrical conductivity step-changed, and for which different
 336 activation energies were found. The transition temperature was ~ 400 °C and was caused by a phase
 337 transition from mixed cubic-tetragonal phases to a pure cubic spinel phase (at high temperatures).
 338 Interestingly, the 03Fe and 05Fe pellets sintered at 1100 °C did not show such a phase transition; only
 339 a slight change of slope of the conductivity curve.

340 Samples with higher iron content showed generally lower conductivity values and a regular thermally
 341 activated behaviour across the full temperature range. For the 03Fe sample, the conductivity was
 342 highest after sintering at 1000 °C; sintering at a higher temperature reduced the conductivity. All of
 343 the other compositions showed an increase of electrical conductivity upon increasing the sintering
 344 temperature. The 03Fe sample showed a conductivity value of ~ 120 S cm^{-1} , whereas the 05Fe sample
 345 had a conductivity of ~ 30 S cm^{-1} at 650 °C. As shown in Figure 6, due to the thermal activation across
 346 the full temperature range, the electrical conductivity of the 03Fe sample became highest for
 347 temperatures above 800 °C. Although the electrical conductivity values clearly depended on the iron
 348 content, they can all be considered relatively high. Based on the results, it can be stated that the
 349 electrical conductivity of the tetragonal phase (the low temperature phase) is greatly reduced in
 350 comparison to the conductivity of the cubic phase.



351
 352 **Figure 6.** Electrical conductivity plot of the 0Fe, 01Fe, 03Fe and 05Fe samples measured on pellets
 353 sintered at 900 °C (a)- results were corrected for sample porosity. Arrhenius plots of electrical

354 conductivity as a function of pellet sintering temperatures (900 °C / 1000 °C / 1100 °C). Results were
 355 not corrected for sample porosity.

356 Based on the Arrhenius plots (Figure 6b–e), the activation energies of the electrical
 357 conductivity were calculated and are presented in Table 3. Due to the visible change in the slopes, the
 358 activation energies were calculated separately for two temperature ranges: 450–650 °C and 200–
 359 400 °C. These two ranges have distinctly different value levels. At high temperatures, the activation
 360 energies were rather low, with values in the range 0.20–0.30 eV and did not seem to depend on the
 361 sintering temperature. At lower temperatures, variation of the activation energies was quite
 362 significant. The lowest values were found for the highest sintering temperature of 1100 °C (between
 363 0.26 eV for the 05Fe sample, and 0.37 eV for the 0Fe) and were only slightly higher than the values
 364 obtained at high temperatures. For lower sintering temperatures, the activation energies were in the
 365 range of 0.4 to 0.7 eV. In general, the obtained values are in agreement with typical reported values
 366 for different spinels [29,30,38]. The difference between the low and high temperature values of the
 367 activation energy may be connected to different grain and grain boundary contributions to the total
 368 electrical conductivity [54].

369

370

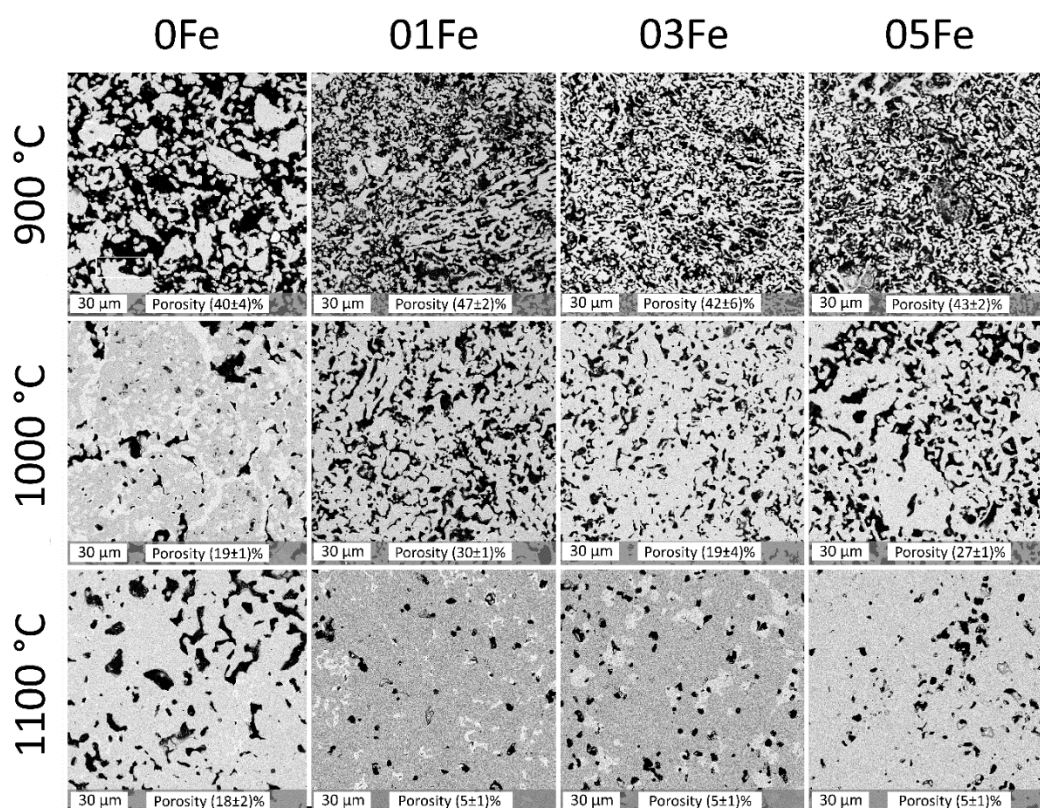
371 **Table 3.** Thermal expansion coefficients of the sintered spinels (from Figure 4c) and activation energy
 372 of the electrical conductivity (E_A) fitted according to Eq. 1 for two temperature ranges (200–400 °C
 373 and 450–650 °C) for each featured material sintered at three temperatures (from Figure 6b–e).

Temperature range	Thermal expansion coefficient TEC [$\times 10^{-6} \text{ K}^{-1}$]		Activation energy for the electrical conductivity E_A [eV]					
	50 °C- 600	600 °C- 900 °C	200 °C - 400 °C			450 °C- 650 °C		
$T_{\text{sintering}}/composition$	1100 °C		900 °C	1000 °C	1100 °C	900 °C	1000 °C	1100 °C
0Fe	9.57	13.01	0.57	0.47	0.37	0.22	0.22	0.25
01Fe	10.15	14.52	0.41	0.43	0.33	0.20	0.21	0.21
03Fe	10.58	18.57	0.53	0.58	0.31	0.21	0.22	0.25
05Fe	9.19	12.81	0.70	0.69	0.26	0.25	0.25	0.27

374

375 **3.3. Microstructural properties of sintered materials**

376 In order to characterise the properties of the materials in more detail, XRD and SEM/EDS
377 analyses of the differently sintered pellets were performed. Images of polished cross-sections of all of
378 the samples are presented in Figure 7, with accompanying elemental maps and chemical compositions
379 in the supplementary materials (Figure S1, Table S1). Based on the images, the porosities of the pellets
380 were determined and the values are included in the figure. The samples sintered at 900 °C showed
381 similar, porous microstructures (porosities ~40–47%). For the samples containing iron, the particle
382 sizes seemed to be smaller than for the non-substituted sample, where large well-sintered structures
383 could be found. For samples sintered at 1000 °C the porosities were considerably lower (~20–30%),
384 and a clear difference in the microstructure was obtained for the 0Fe sample. It was characterised by
385 high density and showed the presence of different phases (different shades of grey). The iron-doped
386 samples showed high density and a small amount of secondary phases. For the samples sintered at
387 1100 °C, the microstructure was quite dense for all samples (porosities 5–20%), and the presence of
388 secondary phases with different chemical compositions were detected for the 0Fe, 01Fe and 03Fe
389 samples in increasing amounts, as can be expected from the XRD data. For the 05Fe sample, no
390 inhomogeneity in the chemical composition was detected by SEM/EDS. XRD analyses of the pellet
391 samples shown in Figure 7 were performed on powders obtained from crushed pellets (XRD spectra
392 are presented in Figure S2). The structural results comply with other data. For a sintering temperature
393 of 900 °C, the phase composition was relatively simple, and pure spinels were obtained (either in cubic,
394 or cubic + tetragonal form) with a minor CuO phase for the 0Fe and 01Fe. Sintering at temperatures of
395 1000 °C and above resulted in the formation of new phases. By analysing the phase diagrams, it can be
396 seen that above 900 °C, the formation of a CuMnO_2 phase started [20], with the formation of a
397 $\text{Cu}_5\text{Mn}_4\text{O}_9$ phase above 975 °C [18]. Generally, based on the results and the published phase diagrams,
398 the structure of the Mn-Cu spinels is retained up to <1000 °C.



399

400

Figure 7. SEM cross-section images of pellets sintered at different temperatures.

401

3.4. General discussion

402

Based on the obtained results, the effect of iron substitution in the Mn-Cu oxide spinel can be discussed. In general, Mn-Cu-based spinels are complex materials, which exhibit quite narrow single-phase regions in phase diagrams. By using a specific Mn:Cu ratio (e.g. 1.7:1.3), it is possible to obtain a pure cubic phase at room temperature, and up to ~600 °C, where CuO starts forming. By adding iron, the stability of the spinel lattice is extended. At room temperature, the 05Fe spinel is a mixture of cubic and tetragonal phases, that upon heating to >400 °C form a single cubic phase, which does not show decomposition into CuO upon further heating. Stabilisation of the spinel phase is important, as for the CuO-containing compositions, reduction to Cu₂O happens at high temperatures. This reduction induces volume changes and can have a negative impact on the material's stability. Due to the precipitation of CuO, the electrical conductivities of the spinels differ. Precipitation of CuO results in lowering of the electrical conductivity, evidenced by a maxima in the conductivity curves, which indicates an important role of copper in the electrical conductivity. By adding Fe, CuO formation is suppressed, and the electrical conductivity follows a pattern expected for a thermally activated semiconductor with visible phase transition to a fully cubic structure.

416

417 3.5. Possible application of the iron-substituted Mn-Cu spinel in solid oxide cells

418 Though not specifically discussed above, iron-substituted spinels are being developed as potential
419 protective coating materials for steel interconnects for high-temperature solid oxide cells. Currently,
420 the state of the art is the MnCo_2O_4 spinel, which shows good protective behaviour, but contains
421 harmful and nonsustainably mined cobalt. Also, there is a strong need for cobalt in the rapidly
422 developing Li-ion market. The results obtained in this work point to the potential applicability of the
423 newly developed materials as protective coatings:

- 424 • Values of the TEC for the spinels might be considered to be compatible with Crofer 22 APU [55]
425 or 441-type ferritic steel [56], which are used for the fabrication of SOFC interconnects;
- 426 • Electrical conductivity of the spinels is sufficiently high at operating temperatures ($> 10 \text{ S cm}^{-1}$
427 at 700–800 °C) [57];
- 428 • Iron substitution improves the sinterability of the spinels. Typically, the coatings are sintered
429 via a reduction and subsequent reoxidation process. Lowering the sintering temperature can
430 help with decreasing the reoxidation temperature from 900 °C [58] to 800°C or time used in
431 coating densification process with the comparison of sintering condition for state of the art
432 Mn_2CoO_4 .
- 433 • Iron-substituted spinels show thermochemical stability in oxidising conditions at high
434 temperatures.

435 To prove the suitability of the materials for protective coatings for steel interconnects, further tests
436 need to be carried out: specifically, issues including optimization of the coating process, sintering
437 conditions, adhesion test, reactivity with Cr, area-specific resistant measurements and long-term
438 corrosion properties (e.g. oxide scale growth kinetics) need to be evaluated. From a materials
439 perspective, however, Fe-modified Mn-Cu spinels seem to have suitable physico-chemical properties
440 for a successful protective coating.

441

442 4. Conclusions

443 In this work, Fe substituted $\text{Mn}_{1.7}\text{Cu}_{1.3-x}\text{Fe}_x\text{O}_4$ spinel-based ceramics ($x=0, 0.1, 0.3, 0.5$) were synthesised
444 and characterised. Adding small amount of Fe ($x = 0.1$) does not alter the properties considerably. On
445 the other hand, adding more iron ($x = 0.3$ or 0.5) results in the formation of the tetragonal spinel due
446 to Jahn-Teller distortion of the octahedra, the change in electrical conductivity properties, and
447 improved stability of the spinel phase (less or no CuO formation). The sinter-activity of the powders is



448 increased with the addition of iron, whereas the thermal expansion remains similar. Iron stabilised the
449 spinel phase, thus no CuO is reduced at high temperatures, and thermal stability of the spinels is
450 improved. The addition of iron results in lowered electrical conductivity. For the 0Fe and 01Fe a
451 maxima in electrical conductivity values were found and correlated to the formation of the CuO phase.
452 For the 03Fe and 05Fe, no maxima were found, and the samples follow a linear, thermally activated
453 behaviour.

454 To conclude, the results show that partial substitution of Cu by Fe in the Mn-Cu spinel leads to
455 suppression of the formation of CuO_x at high temperatures, which improves the thermomechanical
456 properties and sinterability of the ceramics. The concomitant trade-off in electrical properties leaves
457 absolute values of conductivity on the level desirable for SOFC/SOEC applications.

458 **Acknowledgments**

459 This project is supported by National Science Centre (NCN) Harmonia 9 project number UMO-
460 2017/26/M/ST8/00438: “Quest for novel materials for solid oxide cell interconnect coatings”. Funding
461 of WETI PG is also gratefully acknowledged.

462 References

- 463 [1] Q. Zhao, Z. Yan, C. Chen, J. Chen, Spinel: Controlled Preparation, Oxygen
464 Reduction/Evolution Reaction Application, and Beyond, *Chem. Rev.* (2017)
465 *acs.chemrev.7b00051*. <https://doi.org/10.1021/acs.chemrev.7b00051>.
- 466 [2] K.M. Shaju, P.G. Bruce, Nano-LiNi_{0.5}Mn_{1.5}O₄ spinel: a high power electrode for Li-ion
467 batteries, *Dalt. Trans.* 0 (2008) 5471. <https://doi.org/10.1039/b806662k>.
- 468 [3] Y. Zhu, X. Ji, Z. Wu, W. Song, H. Hou, Z. Wu, X. He, Q. Chen, C.E. Banks, Spinel NiCo₂O₄
469 for use as a high-performance supercapacitor electrode material: Understanding of its
470 electrochemical properties, *J. Power Sources.* 267 (2014) 888–900.
471 <https://doi.org/10.1016/J.JPOWSOUR.2014.05.134>.
- 472 [4] S. Chen, X. Zhou, W. Song, J. Sun, H. Zhang, J. Jiang, L. Deng, S. Dong, X. Cao, Mg₂SiO₄
473 as a novel thermal barrier coating material for gas turbine applications, *J. Eur. Ceram. Soc.* 39
474 (2019) 2397–2408. <https://doi.org/10.1016/j.jeurceramsoc.2019.02.016>.
- 475 [5] M. Zawadzki, W. Walerczyk, F.E. López-Suárez, M.J. Illán-Gómez, A. Bueno-López,
476 CoAl₂O₄ spinel catalyst for soot combustion with NO_x/O₂, *Catal. Commun.* 12 (2011) 1238–
477 1241. <https://doi.org/10.1016/J.CATCOM.2011.04.021>.
- 478 [6] S. Takahashi, H. Ogawa, A. Kan, Electronic states and cation distributions of MgAl₂O₄ and
479 Mg_{0.4}Al_{1.6}O₄ microwave dielectric ceramics, *J. Eur. Ceram. Soc.* 38 (2018) 593–598.
480 <https://doi.org/10.1016/j.jeurceramsoc.2017.08.022>.
- 481 [7] H. Jia, W. Zhou, H. Nan, J. Dong, Y. Qing, F. Luo, D. Zhu, Enhanced high temperature
482 dielectric polarization of barium titanate/magnesium aluminum spinel composites and their
483 potential in microwave absorption, *J. Eur. Ceram. Soc.* 40 (2020) 728–734.
484 <https://doi.org/10.1016/j.jeurceramsoc.2019.11.003>.
- 485 [8] Y. Liu, J.W. Fergus, K. Wang, C. Dela Cruz, Crystal Structure, Chemical Stabilities and
486 Electrical Conductivity of Fe-Doped Manganese Cobalt Spinel Oxides for SOFC Interconnect
487 Coatings, *J. Electrochem. Soc.* (2013). <https://doi.org/10.1149/2.114311jes>.
- 488 [9] Y. Zhou, S. Sun, J. Song, S. Xi, B. Chen, Y. Du, A.C. Fisher, F. Cheng, X. Wang, H. Zhang,
489 Z.J. Xu, Enlarged Co–O Covalency in Octahedral Sites Leading to Highly Efficient Spinel
490 Oxides for Oxygen Evolution Reaction, *Adv. Mater.* 30 (2018) 1–7.
491 <https://doi.org/10.1002/adma.201802912>.
- 492 [10] R. Metz, J.P. Caffin, R. Legros, A. Rousset, The preparation, characterization and electrical

- 493 properties of copper manganite spinels, $\text{Cu}_x\text{Mn}_{3-x}\text{O}_4$, $0 \leq x \leq 1$, *J. Mater. Sci.* 24 (1989) 83–
494 87. <https://doi.org/10.1007/BF00660936>.
- 495 [11] G.T. Bhandage, H. V Keer, Structural and magnetic properties of the $\text{Cu}_x\text{Cd}_{1-x}\text{Mn}_2\text{O}_4$
496 system, *J. Phys. C Solid State Phys.* 8 (1975) 501–506.
- 497 [12] G.T. Bhandage, H. V Keer, A correlation of the physical properties of the $\text{Ni}_x\text{Cu}_{1-x}\text{Mn}_2\text{O}_4$
498 system, *J. Phys. C Solid State Phys.* 9 (1976) 1325–1331.
- 499 [13] R. Buhl, Manganites spinelles purs d'elements de transition preparations et structures
500 cristallographiques, *J. Phys. Chem. Solids.* 30 (1969) 805–812. [https://doi.org/10.1016/0022-3697\(69\)90275-3](https://doi.org/10.1016/0022-3697(69)90275-3).
501
- 502 [14] T. Fukunaga, N. Ryumon, N. Ichikuni, S. Shimazu, Characterization of CuMn-spinel catalyst
503 for methanol steam reforming, *Catal. Commun.* 10 (2009) 1800–1803.
504 <https://doi.org/10.1016/j.catcom.2009.06.001>.
- 505 [15] P. Ma, Q. Geng, X. Gao, T. Zhou, S. Yang, G. Liu, Aqueous solution-derived CuMn_2O_4
506 ceramic films for spectrally selective solar absorbers, *Ceram. Int.* (2016).
507 <https://doi.org/10.1016/j.ceramint.2016.09.062>.
- 508 [16] J. Li, C. Xiong, J. Li, D. Yan, J. Pu, B. Chi, L. Jian, Investigation of $\text{MnCu}_0.5\text{Co}_{1.5}\text{O}_4$ spinel
509 coated SUS430 interconnect alloy for preventing chromium vaporization in intermediate
510 temperature solid oxide fuel cell, *Int. J. Hydrogen Energy.* 42 (2017).
511 <https://doi.org/10.1016/j.ijhydene.2017.05.074>.
- 512 [17] F.C.M. Driessens, G.D. Rieck, Phase Equilibria in the System Cu-Mn-O, *J. Inorg. Gen. Chem.*
513 351 (1967) 48–62. <https://doi.org/10.1002/zaac.19673510108>.
- 514 [18] P. Wei, M. Bieringer, L.M.D. Cranswick, A. Petric, In situ high-temperature X-ray and neutron
515 diffraction of Cu-Mn oxide phases, *J. Mater. Sci.* 45 (2010) 1056–1064.
516 <https://doi.org/10.1007/s10853-009-4042-2>.
- 517 [19] C. Maunders, B.E. Martin, P. Wei, A. Petric, G.A. Botton, Investigation of the electronic
518 structure of the cubic spinel $\text{Cu}_{1.2}\text{Mn}_{1.8}\text{O}_4$ using electron energy loss spectroscopy, *Solid*
519 *State Ionics.* 179 (2008) 718–724. <https://doi.org/10.1016/j.ssi.2008.04.029>.
- 520 [20] B.E. Martin, A. Petric, Electrical properties of copper-manganese spinel solutions and their
521 cation valence and cation distribution, *J. Phys. Chem. Solids.* (2007).
522 <https://doi.org/10.1016/j.jpcs.2007.06.019>.
- 523 [21] P. Wei, Spinel coatings for Solid Oxide Fuel Cell interconnects and crystal structure of Cu-Mn-



- 524 O, McMaster University, Canada, 2009.
- 525 [22] A. Petric, H. Ling, Electrical conductivity and thermal expansion of spinels at elevated
526 temperatures, *J. Am. Ceram. Soc.* (2007). <https://doi.org/10.1111/j.1551-2916.2007.01522.x>.
- 527 [23] Z. Sun, R. Wang, A.Y. Nikiforov, S. Gopalan, U.B. Pal, S.N. Basu, CuMn_{1.8}O₄ protective
528 coatings on metallic interconnects for prevention of Cr-poisoning in solid oxide fuel cells, *J.*
529 *Power Sources*. 378 (2018) 125–133. <https://doi.org/10.1016/j.jpowsour.2017.12.031>.
- 530 [24] Z. Sun, S. Gopalan, U.B. Pal, S.N. Basu, Cu_{1.3}Mn_{1.7}O₄ spinel coatings deposited by
531 electrophoretic deposition on Crofer 22 APU substrates for solid oxide fuel cell applications,
532 *Surf. Coatings Technol.* 323 (2017) 49–57. <https://doi.org/10.1016/j.surfcoat.2016.09.028>.
- 533 [25] W. Huang, S. Gopalan, U.B. Pal, S.N. Basu, Evaluation of Electrophoretically Deposited
534 CuMn_{[sub 1.8]O[sub 4]} Spinel Coatings on Crofer 22 APU for Solid Oxide Fuel Cell
535 Interconnects, *J. Electrochem. Soc.* (2008). <https://doi.org/10.1149/1.2975367>.
- 536 [26] P. Zielke, A.C. Wulff, X. Sun, S.H. Jensen, R. Kiebach, H.L. Frandsen, P. Norby, A. Hagen,
537 Investigation of a Spinel-forming Cu-Mn Foam as an Oxygen Electrode Contact Material in a
538 Solid Oxide Cell Single Repeating Unit, *Fuel Cells*. 17 (2017) 730–734.
539 <https://doi.org/10.1002/face.201700005>.
- 540 [27] B. Talic, P.V. Hendriksen, K. Wiik, H.L. Lein, Thermal expansion and electrical conductivity
541 of Fe and Cu doped MnCo₂O₄ spinel, *Solid State Ionics*. 326 (2018) 90–99.
542 <https://doi.org/10.1016/j.ssi.2018.09.018>.
- 543 [28] D. Szymczewska, S. Molin, P. Hendriksen, P. Jasiński, Microstructure and Electrical Properties
544 of Fe,Cu Substituted (Co,Mn)₃O₄ Thin Films, *Crystals*. 7 (2017) 185.
545 <https://doi.org/10.3390/cryst7070185>.
- 546 [29] T. Brylewski, A. Kruk, M. Bobruk, A. Adamczyk, J. Partyka, P. Rutkowski, Structure and
547 electrical properties of Cu-doped Mn-Co-O spinel prepared via soft chemistry and its
548 application in intermediate-temperature solid oxide fuel cell interconnects, *J. Power Sources*.
549 333 (2016) 145–155. <https://doi.org/10.1016/j.jpowsour.2016.09.136>.
- 550 [30] B. Talic, P.V. Hendriksen, K. Wiik, H.L. Lein, Thermal expansion and electrical conductivity
551 of Fe and Cu doped MnCo₂O₄ spinel, *Solid State Ionics*. (2018).
552 <https://doi.org/10.1016/j.ssi.2018.09.018>.
- 553 [31] S. Molin, P. Jasinski, L. Mikkelsen, W. Zhang, M. Chen, P. V. Hendriksen, Low temperature
554 processed MnCo₂O₄ and MnCo_{1.8}Fe_{0.2}O₄ as effective protective coatings for solid oxide fuel

- 555 cell interconnects at 750 °C, *J. Power Sources*. 336 (2016) 408–418.
556 <https://doi.org/10.1016/j.jpowsour.2016.11.011>.
- 557 [32] E. Zanchi, B. Talic, A.G. Sabato, S. Molin, A.R. Boccaccini, F. Smeacetto, Electrophoretic co-
558 deposition of Fe₂O₃ and Mn_{1.5}Co_{1.5}O₄: Processing and oxidation performance of Fe-doped
559 Mn-Co coatings for solid oxide cell interconnects, *J. Eur. Ceram. Soc.* 39 (2019).
560 <https://doi.org/10.1016/j.jeurceramsoc.2019.05.024>.
- 561 [33] S. Molin, A.G. Sabato, H. Javed, G. Cempura, A.R. Boccaccini, F. Smeacetto, Co-deposition
562 of CuO and Mn_{1.5}Co_{1.5}O₄ powders on Crofer22APU by electrophoretic method :
563 Structural , compositional modifications and corrosion properties, *Mater. Lett.* 218 (2018) 329–
564 333. <https://doi.org/10.1016/j.matlet.2018.02.037>.
- 565 [34] N. Grünwald, Y.J. Sohn, X. Yin, N.H. Menzler, O. Guillon, R. Vaßen, Microstructure and
566 phase evolution of atmospheric plasma sprayed Mn-Co-Fe oxide protection layers for solid
567 oxide fuel cells, *J. Eur. Ceram. Soc.* 39 (2019) 449–460.
568 <https://doi.org/10.1016/j.jeurceramsoc.2018.08.027>.
- 569 [35] S. Joshi, A. Petric, Nickel substituted CuMn₂O₄ spinel coatings for solid oxide fuel cell
570 interconnects, *Int. J. Hydrogen Energy*. 42 (2017) 5584–5589.
571 <https://doi.org/10.1016/j.ijhydene.2016.08.075>.
- 572 [36] M. Salavati-Niasari, F. Davar, M. Farhadi, Synthesis and characterization of spinel-type
573 CuAl₂O₄ nanocrystalline by modified sol-gel method, *J. Sol-Gel Sci. Technol.* (2009).
574 <https://doi.org/10.1007/s10971-009-1940-3>.
- 575 [37] J. Lin, Y. He, X. Du, Q. Lin, H. Yang, H. Shen, Structural and Magnetic Studies of Cr³⁺
576 Substituted Nickel Ferrite Nanomaterials Prepared by Sol-Gel Auto-Combustion, *Crystals*. 8
577 (2018) 384. <https://doi.org/10.3390/cryst8100384>.
- 578 [38] M. Bobruk, K. Durczak, J. Dąbek, T. Brylewski, Structure and Electrical Properties of Mn-Cu-
579 O Spinel, *J. Mater. Eng. Perform.* 26 (2017) 1598–1604. <https://doi.org/10.1007/s11665-017-2588-8>.
- 581 [39] Z. Sun, S. Gopalan, U.B. Pal, S.N. Basu, Cu_{1.3}Mn_{1.7}O₄ spinel coatings deposited by
582 electrophoretic deposition on Crofer 22 APU substrates for solid oxide fuel cell applications,
583 *Surf. Coatings Technol.* (2017). <https://doi.org/10.1016/j.surfcoat.2016.09.028>.
- 584 [40] M. Bobruk, K. Brylewska, K. Durczak, K. Wojciechowski, A. Adamczyk, T. Brylewski,
585 Synthesis of manganese-cobalt spinel via wet chemistry methods and its properties, *Ceram. Int.*
586 43 (2017) 15597–15609. <https://doi.org/10.1016/j.ceramint.2017.08.116>.

- 587 [41] W. -S Hong, L.C. De Jonghe, X. Yang, M.N. Rahaman, Reaction Sintering of ZnO-Al₂O₃, J.
588 Am. Ceram. Soc. (1995). <https://doi.org/10.1111/j.1151-2916.1995.tb07957.x>.
- 589 [42] J. Marín-Romero, L. Fuentes-Cobas, J. Rodríguez-Carvajal, C. Tabasco-Novelo, P. Quintana,
590 Structure of a Novel Spinel Li_{0.5}Zn_{5/3}Sb_{2.5/3}O₄ by Neutron and Synchrotron Diffraction
591 Analysis, Crystals. 7 (2017) 280. <https://doi.org/10.3390/cryst7090280>.
- 592 [43] A.E. Danks, S.R. Hall, Z. Schnepf, The evolution of “sol-gel” chemistry as a technique for
593 materials synthesis, Mater. Horizons. (2016). <https://doi.org/10.1039/c5mh00260e>.
- 594 [44] M. Galceran, · M C Pujol, · M Aguiló, · F Díaz, M. Aguiló, F. Díaz, Sol-gel modified Pechini
595 method for obtaining nanocrystalline KRE(WO₄)₂ (RE = Gd and Yb) Sol-gel modified Pechini
596 method for obtaining nanocrystalline KRE(WO₄)₂ (RE = Gd and Yb), Artic. J. Sol-Gel Sci.
597 Technol. 42 (2007) 79–88. <https://doi.org/10.1007/s10971-006-1517-3>.
- 598 [45] C.W. Bale, E. Bélisle, P. Chartrand, S.A. Deckerov, G. Eriksson, A.E. Gheribi, K. Hack, I.H.
599 Jung, Y.B. Kang, J. Melançon, A.D. Pelton, S. Petersen, C. Robelin, J. Sangster, P. Spencer,
600 M.A. Van Ende, FactSage thermochemical software and databases, 2010-2016, Calphad
601 Comput. Coupling Phase Diagrams Thermochem. 54 (2016) 35–53.
602 <https://doi.org/10.1016/j.calphad.2016.05.002>.
- 603 [46] L.J. van der Pauw, A method of measuring the resistivity and Hall coefficient on samples of
604 arbitrary shape, Philips Res. Reports. (1958).
605 <https://doi.org/537.723.1:53.081.7+538.632:083.9>.
- 606 [47] R. Landauer, Electrical conductivity in inhomogeneous media, in: AIP Conf. Proc., AIP
607 Publishing, 2008: pp. 2–45. <https://doi.org/10.1063/1.311150>.
- 608 [48] A. Purwanto, A. Fajar, H. Mugirahardjo, J.W. Fergus, K. Wang, Cation distribution in spinel
609 (Mn,Co,Cr)O₄ at room temperature, J. Appl. Crystallogr. 43 (2010) 394–400.
610 <https://doi.org/10.1107/S0021889810008150>.
- 611 [49] H.A. Jahn, E. Teller, Stability of polyatomic molecules in degenerate electronic states - I—
612 Orbital degeneracy, Proc. R. Soc. 161 (1937) 220–235.
- 613 [50] J.D. Dunitz, L.E. Orgel, Electronic properties of transition-metal oxides—I. Distortions from
614 cubic symmetry, J. Phys. Chem. Solids. 3 (1957) 20–29. [https://doi.org/10.1016/0022-3697\(57\)90043-4](https://doi.org/10.1016/0022-3697(57)90043-4).
- 615
616 [51] N. Baffier, M. Huber, Etude par diffraction des rayons X et des neutrons, des relations entre
617 distribution cationique et distorsion cristalline dans les ferro-manganites spinelles: xMnO₃ +



- 618 (1 - x) Cu(Fe,Cr)2O4, *J. Phys. Chem. Solids.* 33 (1972) 737–747. [https://doi.org/10.1016/0022-](https://doi.org/10.1016/0022-3697(72)90081-9)
619 3697(72)90081-9.
- 620 [52] Y. Zhu, K. Mimura, M. Isshiki, Oxidation mechanism of Cu2O to CuO at 600-1050 °C, *Oxid.*
621 *Met.* 62 (2004) 207–222. <https://doi.org/10.1007/s11085-004-7808-6>.
- 622 [53] T. Narushima, H. Tsukamoto, T. Yonezawa, High temperature oxidation event of gelatin
623 nanoskin-coated copper fine particles observed by in situ TEM, *AIP Adv.* 2 (2012).
624 <https://doi.org/10.1063/1.4759498>.
- 625 [54] N. Ponpandian, P. Balaya, A. Narayanasamy, Electrical conductivity and dielectric behaviour
626 of nanocrystalline NiFe₂O₄ spinel, *J. Phys. Condens. Matter.* 14 (2002) 3221–3237.
627 <https://doi.org/10.1088/0953-8984/14/12/311>.
- 628 [55] M. Stygar, K. Matsuda, S. Lee, T. Brylewski, Corrosion Behavior of Crofer 22APU for
629 Metallic Interconnects in Single and Dual Atmosphere Exposures at 1073 K, 131 (2017).
630 <https://doi.org/10.12693/APhysPolA.131.1394>.
- 631 [56] Stainless Steel Type 441 – Rolled Metal Products | Stainless, Aluminum & Specialty Alloys,
632 (n.d.). <https://rolledmetalproducts.com/stainless-steel-type-441/> (accessed March 9, 2020).
- 633 [57] C. Goebel, A.G. Fefekos, J.E. Svensson, J. Froitzheim, Does the conductivity of interconnect
634 coatings matter for solid oxide fuel cell applications?, *J. Power Sources.* 383 (2018) 110–114.
635 <https://doi.org/10.1016/j.jpowsour.2018.02.060>.
- 636 [58] M. Bobruk, S. Molin, M. Chen, T. Brylewski, P. V. Hendriksen, Sintering of
637 MnCo2O4 coatings prepared by electrophoretic deposition, *Mater. Lett.* (2018).
638 <https://doi.org/10.1016/j.matlet.2017.12.046>.
- 639